

See discussions, stats, and author profiles for this publication at: <https://www.researchgate.net/publication/280056853>

Coordinative Crystallization of ZrSiO₄ and α -Fe₂O₃ Composites and Their Resultant Structural, Morphological, and Mechanical Characteristics

ARTICLE in CRYSTAL GROWTH & DESIGN · JULY 2015

Impact Factor: 4.89 · DOI: 10.1021/acs.cgd.5b00677

READS

94

3 AUTHORS:



[Udaykiran Roopavath](#)

Indian Institute of Technology Hyderabad

2 PUBLICATIONS 0 CITATIONS

[SEE PROFILE](#)



[Vasanthavel Subramaniyan](#)

Pondicherry University

8 PUBLICATIONS 8 CITATIONS

[SEE PROFILE](#)



[Kannan Sanjeevi](#)

20 PUBLICATIONS 35 CITATIONS

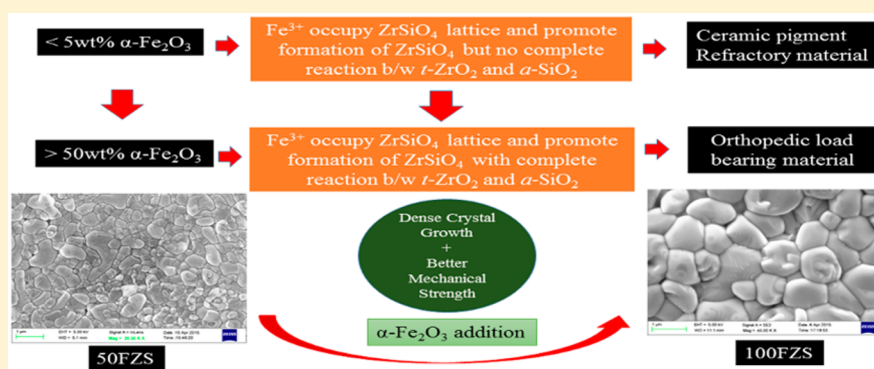
[SEE PROFILE](#)

Coordinative Crystallization of ZrSiO_4 and $\alpha\text{-Fe}_2\text{O}_3$ Composites and Their Resultant Structural, Morphological, and Mechanical Characteristics

Roopavath Udaykiran, Subramaniyan Vasanthavel, and Sanjeevi Kannan*

Centre for Nanoscience and Technology, Pondicherry University, Puducherry-605 014, India

Supporting Information



ABSTRACT: The present study investigates the formation of zircon (ZrSiO_4) and hematite ($\alpha\text{-Fe}_2\text{O}_3$) biphasic composites targeted for biomedical applications. The main aim of this study is to understand the role of $\alpha\text{-Fe}_2\text{O}_3$ in controlling the ZrSiO_4 crystallization followed by their mechanical evaluation. The results from the investigation confirmed the essential role of both the heat treatment conditions and $\alpha\text{-Fe}_2\text{O}_3$ content in the elimination of $t\text{-ZrO}_2$, $c\text{-SiO}_2$, and $m\text{-ZrO}_2$ phases to yield composite mixtures of ZrSiO_4 and $\alpha\text{-Fe}_2\text{O}_3$. The occupancy of Fe^{3+} at the Zr^{4+} sites of ZrSiO_4 lattice has stimulated the interfacial reaction between amorphous SiO_2 and $t\text{-ZrO}_2$ to yield crystallized ZrSiO_4 . $\alpha\text{-Fe}_2\text{O}_3$ content in the concentration range of 50–100 wt % was sufficient enough to achieve the formation of biocompatible $\text{ZrSiO}_4/\alpha\text{-Fe}_2\text{O}_3$ composite at 1300 °C with the yield of better mechanical properties.

INTRODUCTION

The mineral zircon (ZrSiO_4) occurs in low concentration, as an accessory mineral, in a wide variety of naturally occurring rocks. ZrSiO_4 is an important raw material and is highly investigated in geochemical sciences, as it acts as a host for radioactive elements like thorium and uranium and also many heavy rare earth elements. In the binary $\text{SiO}_2\text{-ZrO}_2$ system, the only crystalline phase of ZrSiO_4 is stable after 1676 °C. Because of the ability of zircon in offering high resistance to melt corrosion, its attractive thermal and mechanical properties are of considerable value in promoting its use in the manufacture of refractories and as vigorous enamels and pottery glazes. The purity of ZrSiO_4 is a major concern in exploring these fascinating properties for high temperature applications. Natural ZrSiO_4 sand is always prone to impurities such as alumina (Al_2O_3), titania (TiO_2), and silica (SiO_2), which show their effect by changing the mechanical properties and decreasing the decomposition temperature. Researchers have reported the formation of pure ZrSiO_4 by simple sol–gel synthesis via an aqueous semialkoxide route.^{1–4} Low temperature synthesis of ZrSiO_4 powders can also be achieved with the aid of mineralizers, but the use of mineralizer is found to be expensive and hazardous as most of them are toxic. Inclusion of

iron as a dopant in the $\text{SiO}_2\text{-ZrO}_2$ binary system has promoted the formation of ZrSiO_4 at low temperatures but with traces of tetragonal zirconia ($t\text{-ZrO}_2$) in it. This trace of $t\text{-ZrO}_2$ is expected to leach zirconium ion (Zr^{4+}) with a rise in temperature leading to its thermal decomposition which is not favorable for high temperature applications.^{5,6} On the other hand, addition of a small amount of iron has enhanced the optical properties of ZrSiO_4 making it a promising pink-colored pigmenting material for high temperature ceramic pigment applications. Shapes and sizes of this kind of ZrSiO_4 based pigmenting ceramics were also controlled by using different reaction environments and chemical reagents.^{7,8} Vanadium doped ZrSiO_4 powders were also synthesized using the sol–gel route for blue-colored pigmenting applications.⁹

The magnetic, dielectric, optical, catalytic, and photocatalytic properties of hematite ($\alpha\text{-Fe}_2\text{O}_3$) have been widely investigated for electronic and photoelectrochemical applications over the past few decades. $\alpha\text{-Fe}_2\text{O}_3$ has also been reported in the literature because its much lower biotoxicity makes it a

Received: May 15, 2015

Revised: June 18, 2015

promising material for biomedical and drug delivery applications.^{10–12} In a study reported by Heydari et al., $\alpha\text{-Fe}_2\text{O}_3$ – ZrSiO_4 nanocomposites with Fe/Zr molar ratio of 5–30% was synthesized from alkoxide precursors of Si and Zr by the sol-gel method.¹³ In this report, $\alpha\text{-Fe}_2\text{O}_3$ nanoparticles were included in the ZrSiO_4 matrix in order to increase its stability. Hosseini-Zori studied the microstructure of nanohematite encapsulated by ZrSiO_4 and crystobalite ($c\text{-SiO}_2$) for ceramic pigment and glazing applications.¹⁴ The synthesis of composite ceramic material containing pure ZrSiO_4 phase as a host matrix by using simple chemical routes is found lacking in the literature. The use of ZrSiO_4 as a load-bearing material for orthopedic and biomedical applications, despite its extraordinary mechanical properties, is not greatly explored in the literature. The formation and application of pure $\text{ZrSiO}_4\text{-}\alpha\text{-Fe}_2\text{O}_3$ composites for biomedical and bioinorganic applications has not yet been reported so far. In an attempt to obtain such a pure ZrSiO_4 host matrix without any impure phases, continuous addition of substantial amounts of Fe_2O_3 in the $\text{SiO}_2\text{-ZrO}_2$ binary system is investigated and the resultant mechanical properties and biocompatibility are determined in the present study targeting their use as a bone or dental implant in load-bearing applications. This report aims to enhance the scope of these biphasic composites by proposing their use as a vital biomaterial, which can be used for fabricating a wide variety of biomedical devices.

EXPERIMENTAL SECTION

Powder Synthesis. Sol-gel technique was employed to synthesize 6 different $\text{ZrSiO}_4\text{-}\alpha\text{-Fe}_2\text{O}_3$ composites in accordance with some minor modifications in the procedure as explained by the authors in their previous reports.^{15,16} For this purpose, analytical grade zirconium oxychloride octahydrate [$\text{ZrOCl}_2\text{·8H}_2\text{O}$, Hi-Media, India], tetraethyl orthosilicate [$(\text{C}_2\text{H}_5)_4\text{OSi}$, TEOS, Sigma-Aldrich, India], and ferric nitrate nanohydrate [$\text{Fe}(\text{NO}_3)_3\text{·9H}_2\text{O}$, Sigma-Aldrich, India] were used as precursors. The molar concentrations of all the precursors and their sample codes are presented in Table 1. The synthesis procedure is explained in brief as follows: 0.5 mol of TEOS was dissolved in ethanol under constant stirring for 15 min. Separately prepared solution mixtures containing $\text{Fe}(\text{NO}_3)_3$ and ZrOCl_2 were added one after

another to the completely dissolved TEOS solutions under constant stirring conditions. 1.5 mL of HNO_3 was now added to the solution mixtures and reaction was kept under constant stirring at 60 °C with a rotation speed of 250 rpm until the formation of a semisolid gel. These semisolid gels were transferred to a hot air oven and dried at 120 °C overnight. The obtained dried gels were ground to fine powders for any further analysis.

Powder Characterization. The as-dried powders were subjected to heat treatments at varied temperatures with a dwelling time of 4 h to observe any changes in phase behavior and crystallization. XRD studies for all the powders were carried out using a high-resolution RIGAKU, ULTIMA IV, X-ray diffractometer with $\text{Cu K}\alpha$ radiation ($\lambda = 1.5406 \text{ nm}$) produced at 40 kV and 30 mA to scan the diffraction angles (2θ) between 10° and 70° with a step size of 0.02° 2θ per second. Phase determinations were made using Standard ICDD (International Centre for Diffraction Data) card no. 01–083–1378 for ZrSiO_4 , 01–083–0944 for monoclinic zirconia ($m\text{-ZrO}_2$), 01–076–8401 for $\alpha\text{-Fe}_2\text{O}_3$, 01–078–1765 for tetragonal zirconia ($t\text{-ZrO}_2$), and 00–039–1425 for crystobalite ($c\text{-SiO}_2$). Fourier transform infrared (FT-IR) spectra for the powders (NICOLET iS10, FT-IR spectrophotometer, USA) were recorded to determine the vibrational modes in the infrared region. For this purpose each powder was mixed with potassium bromide (KBr) in the proportion of 1/150 (by weight) and pressed into a pellet. Raman spectra for the powders were recorded using a confocal Raman microscope (RENISHAW, United Kingdom). All the powder samples were excited at a wavelength of 785 nm by semiconductor diode laser (0.5% of power) with a data acquiring time of 30 s. The preferred scans for all the powder samples were done in the range of 100–1200 cm^{-1} and all the analyses were done at room temperature.

Quantitative Analysis by Rietveld Refinement. Rietveld method using GSAS-EXPGUI software package was employed to perform the quantitative analysis.^{17,18} Quantitative refinement was carried out for all the powder samples after heat treatment at specific temperatures. All the standard crystallographic information files were obtained from the American Mineralogist crystal structure database. The standard crystallographic data for the refinement of ZrSiO_4 , $\alpha\text{-Fe}_2\text{O}_3$, $t\text{-ZrO}_2$, $m\text{-ZrO}_2$, and $c\text{-SiO}_2$ were, respectively, obtained from Hazen and Finger,¹⁹ Blake and Hessevick,²⁰ Howard et al.,²¹ Smith and Newkirk,²² and Dera et al.²³ The quantitative analysis, weight fraction, and structural parameters of the powders were determined by evaluating numerous cycles in the process of structural refinement. Literature values are used to fix the structural parameters in the first step of the refinement. Then, during the successive refinement cycles numerous parameters were allowed to vary according to the relative weight amount of the observed phases. The following refinement sequence has been used as a standard for all the structures: scale factor, zero shift, background as Chebyshev polynomial of fifth grade, peak profile, and lattice parameters. Fittings were performed using pseudo-Voigt peak profile functions and a preferred orientation along [001] was taken into account with the Marsh model. The fractional coordinates, isotropic temperature, and atomic parameters were employed during refinement.

Cytotoxicity Tests. The cytotoxicity tests for pure ZS and the selected $\text{ZrSiO}_4\text{-}\alpha\text{-Fe}_2\text{O}_3$ composite (50 FZS and 100 FZS) powder samples were performed on the human Osteosarcoma cell line, MG-63, by using MTT assay. Cytotoxicity assessments were made according to the protocol explained in ISO 10993–5.²⁴ The MG-63 cell line was obtained from National Centre for Cell Science, India and the cells were maintained and cultured in Dulbecco's modified Eagle's medium with 10% fetal calf serum at 37 °C at 5% CO_2 . For MTT assay, 10 000 cells were seeded in 96 well culture plates and incubated with or without the indicated amount of sterile 50 FZS, 100 FZS, and pure ZS (control) for 96 h. The drug MG-132 (Sigma-Aldrich) was included in the assay as a positive control, which is a potent proteosomal inhibitor and is known to induce apoptosis.^{25,26} After the incubation, the MTT assay was performed using EZ count MTT cell assay kit (Himedia, Cat. No. CCK003) as per the manufacturer's instructions. MTT assay was performed with triplicate samples to

Table 1. Molar Concentrations of the Precursors Used in the Synthesis

sample code	molar concentrations of the precursors			Zr/Si molar ratio	wt % of Fe with respect to Zr
	ZrOCl ₂	TEOS	Fe(NO ₃) ₃		
Pure ZS	0.500 M	0.500 M	-	1.0	-
	^a 8.056 g	^a 5.582 mL	-		
5 FZS	0.500 M	0.500 M	0.025 M	1.0	5%
	^a 8.056 g	^a 5.582 mL	^a 1.010g		
10 FZS	0.500 M	0.500 M	0.050 M	1.0	10%
	^a 8.056 g	^a 5.582 mL	^a 2.020g		
20 FZSg	0.500 M	0.500 M	0.100 M	1.0	20%
	^a 8.056 g	^a 5.582 mL	^a 4.040g		
50 FZS	0.500 M	0.500 M	0.250 M	1.0	50%
	^a 8.056 g	^a 5.582 mL	^a 10.101 g		
75 FZS	0.500 M	0.500 M	0.375 M	1.0	70%
	^a 8.056 g	^a 5.582 mL	^a 15.150 g		
100 FZS	0.500 M	0.500 M	0.500 M	1.0	100%
	^a 8.056 g	^a 5.582 mL	^a 20.202 g		

^aDenotes the amount of reagent used for 100 mL of solvent.

ensure reproducibility. Data are presented as means \pm standard deviation.

The percentage of cell viability was calculated with respect to control as follows:

$$\text{Cell viability}(\%) = \frac{\text{Intensity}_{\text{sample}}}{\text{Intensity}_{\text{control}}} \times 100 \quad (2)$$

where $\text{Intensity}_{\text{sample}}$ and $\text{Intensity}_{\text{control}}$ represent the optical density (OD) values of cells incubated with sample and culture medium, respectively.

Mechanical Studies. The nanoindentation measurements for the selected compositions (50FZS and 100FZS) were carried out at room temperature using a Nanoindenter machine (Bruker, USA). For this purpose, the as-dried powders were initially heat-treated at 900 °C to eliminate all the volatile impurities followed by milling with ZrO₂ balls for 2 h (Retsch, Germany). The milled powders were pressed in the form of pellets (10 mm diameter and 1 mm thickness) using a semiautomatic hydraulic press machine (Kimaya Engineers, India) under the applied force of 10 N for 60 s. The pellets thus obtained were heat-treated at 1300 °C for 4 h followed by fine polishing using diamond paste and were subjected to mechanical tests. The indentation procedure to determine the mechanical properties was performed according to the standard described by Oliver and Pharr.²⁷ Hardness and Young's Modulus were derived by applying two different loads (50 mN and 100 mN) at multiple positions and the resultant load versus depth profiles was obtained. A triangular pyramid (Berkovich) diamond tip indenter with a radius of curvature of 50 nm was used. In the nanoindentation method, the selected mechanical properties such as Young's modulus and hardness were evaluated using a conventional depth-sensing test, where the measurement cycle (load/unload–displacement curves) consists of a loading segment followed by a dwell time at maximum load and finally an unloading segment. At least three different pellets of the same composition were subjected to testing and all the pellets were analyzed through single indent mode with 5 indents for each pellets at random locations. The surface morphological features of the pellets heat-treated at 1300 °C prior to diamond polishing were determined by FE-SEM (field emission scanning electron microscopy, Carl Zeiss, Germany).

RESULTS

XRD Analysis. The XRD patterns of the powder compositions after heat treatment at 800 °C (Figure 1) and 900 °C (figure not presented) indicated the formation of *t*-ZrO₂. The X-ray reflections that correspond to the formation of α -Fe₂O₃ were determined at 800 °C for the samples that

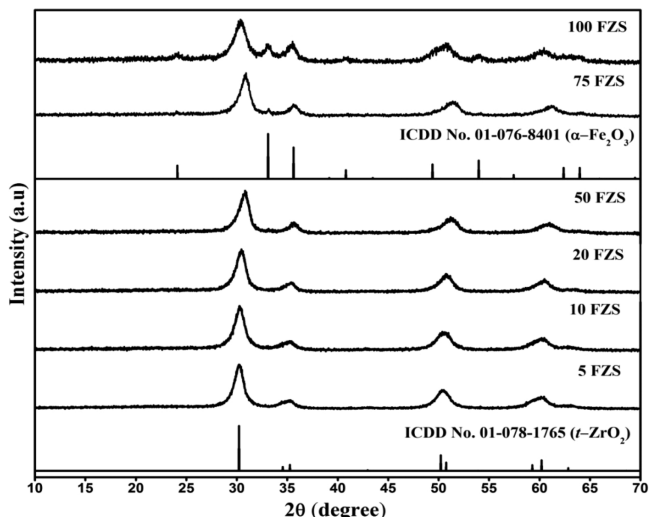


Figure 1. XRD patterns recorded for all the compositions at 800 °C.

possessed higher iron content (75 FZS and 100 FZS). No sign of ZrSiO₄ crystallization is observed until the heat treatment of 900 °C. The XRD patterns at 1000 °C indicated enhancement in the crystallinity of *t*-ZrO₂ and α -Fe₂O₃ by the virtue of appearance of sharp peaks for the respective phases. The reflections that corresponds to the ZrSiO₄ crystallization is determined at 1000 °C (Figure 2); however, the reflections

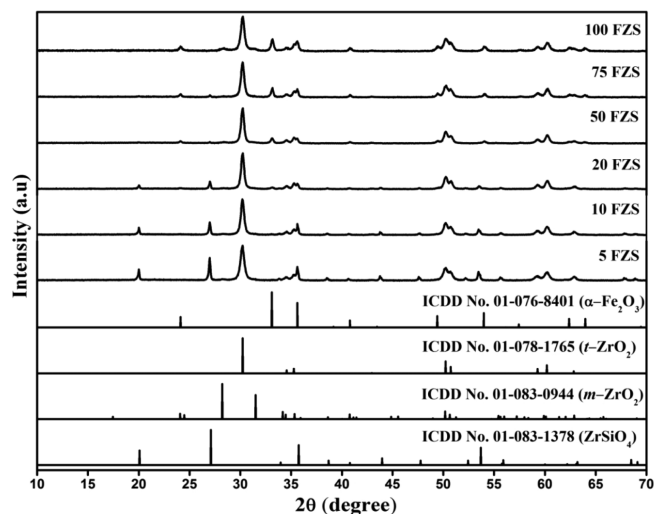


Figure 2. XRD patterns recorded for all the compositions at 1000 °C.

pertaining to ZrSiO₄ formation showed a decreasing trend with the increasing reflections of α -Fe₂O₃. A major change in the phase behavior is noted after heat treatment at 1100 °C (Figure 3) in which the dominant *t*-ZrO₂ and recessive ZrSiO₄

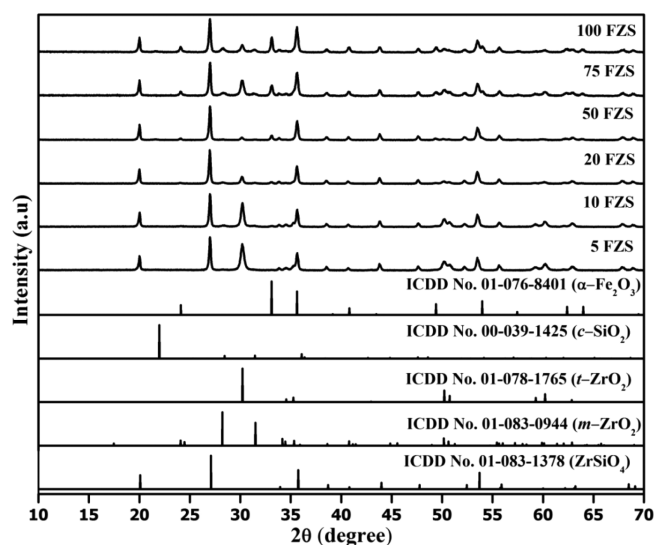


Figure 3. XRD patterns recorded for all the compositions at 1100 °C.

reflections determined at 1000 °C resulted in the formation of X-ray reflections in a reversible manner. Moreover, the existence of a trace level of *m*-ZrO₂ phase is determined at 1100 °C. Progressive heat treatments at 1200 °C (figure not presented) and 1300 °C (Figure 4) resulted in the gradual decline of peaks pertaining to the *t*-ZrO₂ phase leading to its complete loss at 1300 °C for the samples that contained higher α -Fe₂O₃ (50 FZS, 75 FZS, 100 FZS). However, the samples containing lower α -Fe₂O₃ concentrations (5 FZS, 10 FZS, 20

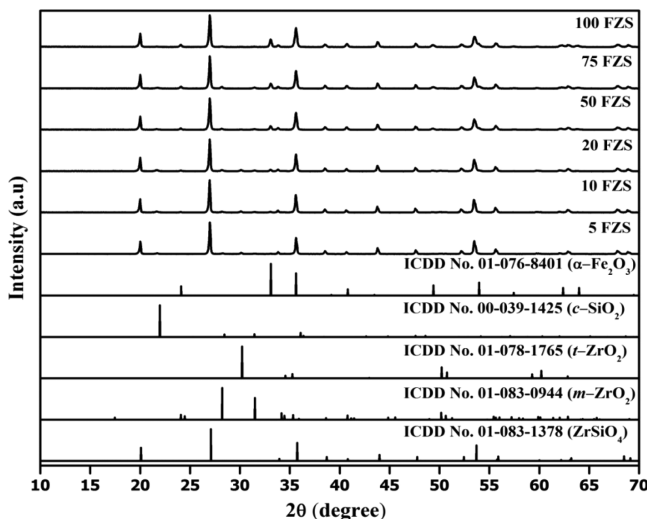


Figure 4. XRD patterns recorded for all the compositions at 1300 °C.

FZS) still indicated the presence of minor peaks pertaining to *m*-ZrO₂, *m*-ZrO₂, and *c*-SiO₂ phases at 1300 °C.

Quantitative Analysis. Quantitative analysis of the X-ray powder diffraction data using Rietveld refinement was performed for selected temperatures. The refined structural data for the different heat treatment temperatures are presented in Table 2. Figures 5 and 6 show the Rietveld plot of X-ray powder diffraction data for SFZS (1200 °C) and 7SFZS (1300 °C), respectively. The lattice parameters of the ZrSiO₄ [tetragonal setting, space group *I41/amd*(141)], *t*-ZrO₂ [tetragonal setting, space group *P42/nmc*(137)], α-Fe₂O₃ [trigonal setting, space group *R*̄*3**c*(167)] confirmed their respective crystal structures. The lattice parameters of trace phases like *m*-ZrO₂ and *c*-SiO₂ were not taken into account because of their detection in low phase fractions at all the temperatures. The refined structural parameters (Table 2, Figure 7a) for the ZrSiO₄ phase showed lattice contraction with respect to the increasing occurrence of α-Fe₂O₃ in the composite system. Such inference signifies the fact that ZrSiO₄ has suffered structural defects due to the inclusions of Fe³⁺ at its lattice. To confirm this fact, the occupancy factors were refined for testing any kind of possible Fe³⁺ inclusions at ZrSiO₄ lattice and the refined occupancy values confirmed the Fe³⁺ occupancy at Zr⁴⁺ site of ZrSiO₄ lattice. The increasing occupancy values (Figure 7a) with respect to the increasing iron content were evident from the results. The selected bond lengths presented in Figure 7b also confirms the steady decline in Zr–O bond lengths with respect to the increased iron concentration. Thus, the occupancy of the smaller-sized Fe³⁺ for larger-sized Zr⁴⁺ has led to the lattice contraction of ZrSiO₄ and this resulted in the steady decline of Zr–O bond lengths. The phase fractions of multiple phases determined from refinement imply the significance of phase changes in composite system during heat treatment. The gradual conversion of *t*-ZrO₂ to ZrSiO₄ with the increment in heat treatments was found inevitable from the observed results. It has been reported by the authors that for the pure SiO₂–ZrO₂ system, *t*-ZrO₂ phase is retained until 1100 °C and its degradation to yield *m*-ZrO₂ and *c*-SiO₂ was found inevitable at 1200 °C.¹⁵ Thus, the α-Fe₂O₃ content has played a crucial role in preventing the system from degradation in which the systems with low α-Fe₂O₃ (5 FZS, 10 FZS, 20 FZS) has

resulted in the formation of *m*-ZrO₂ and *c*-SiO₂ whereas the systems with considerable α-Fe₂O₃ (50 FZS, 75 FZS, 100 FZS) have restricted the formation of *m*-ZrO₂ and *c*-SiO₂ at all the investigated temperatures.

Raman Spectra. The Raman spectra recorded at 1100 °C (Figure 8) and 1300 °C (Figure 9) confirm the presence of both ZrSiO₄ and α-Fe₂O₃ phases. The peaks that correspond to the presence of *t*-ZrO₂ (146, 270, 320, 459, and 646 cm⁻¹) are determined at 1100 °C for the samples containing low α-Fe₂O₃ content, namely, SFZS, 10 FZS, and 20 FZS.²⁸ The characteristic presence of both ZrSiO₄ and α-Fe₂O₃ phases is significant in all samples at 1100 and 1300 °C. The characteristic nature of ZrSiO₄ is determined from the bands observed at 201, 214, 356, 439, 974, and 1007 cm⁻¹.^{29,30} The presence of the α-Fe₂O₃ phase is confirmed from the observed bands at 227, 244, 490, and 602 cm⁻¹.³¹

FTIR Analysis. FTIR spectra recorded at 900 °C (Figure 10) indicated a characteristic band for Si–O–Si stretching at 830 cm⁻¹. At 900 °C, a broad stretch in the range 980–1280 cm⁻¹ characteristic of Zr–O–Si and Si–O–Si bonds (LO and TO asymmetric stretching modes) is witnessed for the SFZS sample. This broad 980–1280 cm⁻¹ band indicated a sharp shift in the form of narrowed spectrum with increasing α-Fe₂O₃ content. The 980 and 1280 cm⁻¹ band showed respective strong shift toward 1060 and 1200 cm⁻¹ for the sample that contains higher α-Fe₂O₃ content (100FZS). The band determined at 1630 cm⁻¹ is assigned for the surface adsorbed OH groups, and the observed bands at 1870 and 1960 cm⁻¹ are attributed for the vibrations of SiO₂ network. The intensity of the bands at 1870 and 1960 cm⁻¹ indicated a steady decline with respect to the increasing α-Fe₂O₃ content and finally gets diminished for 100FZS sample. In 100FZS sample, new bands are detected at 440 and 630 cm⁻¹ that corresponds to the Si–O–Si bonds and Fe–O stretching vibrations, respectively.³²

The formation of highly crystalline ZrSiO₄ phase at 1300 °C (Figure 11) is confirmed from the bands observed at 432, 617, 880, and 1028 cm⁻¹.^{33,34} As observed for the SFZS sample at 900 °C, the band that corresponds to Si–O–Si asymmetric stretching observed at 1200 cm⁻¹ has indicated a shift toward lower frequency with increasing α-Fe₂O₃ content. Additional bands detected at 480 and 560 cm⁻¹ in 1300 °C heat treated samples can be assigned to the presence of α-Fe₂O₃.³² The shoulder band at 480 cm⁻¹ is determined only for the samples that contained higher α-Fe₂O₃ content.

Cytotoxicity effect. The results of the cytotoxicity tests performed on MG-63 cell line by MTT assay are illustrated in Figure 12. The interaction between the ZrSiO₄–α-Fe₂O₃ composite material and the cells were found apparent from the results. The minimum limit of good cell viability using this assay was 65%,³⁵ and the cell viability on both the compositions and on all extract dilutions was found greater than 95%. The bioinert behavior of ZS system is maintained even at higher iron concentrations as evident from cell viability results. The cell viability is expected to decrease with higher additions of Fe³⁺, as larger amounts of α-Fe₂O₃ comes in contact with the cells especially in the case of 100 FZS. The absence of any such inference may be due to the excellent integration of α-Fe₂O₃ in ZrSiO₄ matrix, because of which the reduced cytotoxic effect is observed. The positive role of silica (SiO₂) in bone integration and cell proliferation and the role of Fe₂O₃ in cytotoxicity has been reported in the literature.^{36,37} Nevertheless, further detailed studies are required to understand the cytotoxicity mechanisms of ZrSiO₄–α-Fe₂O₃ composites.

Table 2. Structural Parameters and Phase Fractions Determined from Rietveld Refinement

sample code	χ^2	R_p (%)	R_{Bragg}	ZrSiO ₄	1000 °C				lattice data for ZrSiO ₄ and ^a α -Fe ₂ O ₃	
					Fe ₂ O ₃	t-ZrO ₂	m-ZrO ₂	c-SiO ₂	$a = b$ = axis (Å)	c = axis (Å)
5 FZS	1.385	05.83	04.86	30.73	0	65.34	3.91	-	6.6047 (3)	5.9830 (3)
10 FZS	1.146	05.52	04.12	23.69	1.4	71.96	2.93	-	6.6000 (3)	5.9789 (3)
20 FZS	1.158	05.73	03.45	13.34	8.81	71.18	6.66	-	^a 5.0421 (4)	^a 13.7935 (1)
50 FZS	1.120	05.60	05.43	4.00	28.12	65.89	1.98	-	6.5984 (4)	5.9782 (5)
75 FZS	1.127	06.48	06.09	2.41	31.01	63.81	2.76	-	^a 5.0441 (6)	^a 13.7517 (4)
100 FZS	1.121	06.60	04.57	2.02	35.38	57.68	4.91	-	6.5974 (4)	5.9774 (5)
									^a 5.0405 (4)	^a 13.7465 (2)
									^a 5.0379 (3)	^a 13.7463 (1)
									6.5956 (1)	5.9757 (4)
									6.5938 (4)	5.9734 (5)
									^a 5.0378 (4)	^a 13.7437 (2)
1100 °C										
sample code	χ^2	R_p (%)	R_{Bragg}	ZrSiO ₄	phase fraction (%)				lattice data for ZrSiO ₄ and ^a α -Fe ₂ O ₃	
					Fe ₂ O ₃	t-ZrO ₂	m-ZrO ₂	c-SiO ₂	$a = b$ = axis (Å)	c = axis (Å)
5 FZS	1.418	05.99	03.07	53.33	0	46.66	0	-	6.6118(3)	5.9896 (3)
10 FZS	1.012	05.00	02.51	51.91	4.86	36.25	6.97	-	6.6042 (2)	5.9833 (2)
20 FZS	1.640	06.56	02.39	60.01	8.01	22.94	9.03	-	^a 5.0550 (3)	^a 13.7431(3)
50 FZS	1.611	07.13	03.30	50.23	18.56	25.76	5.44	-	6.5984 (2)	5.9773 (2)
75 FZS	1.240	06.59	02.88	41.13	26.8	25.19	6.87	-	^a 5.0487 (3)	^a 13.7687 (4)
100 FZS	1.245	06.87	02.71	39.6	31.67	19.17	9.55	-	6.5967 (2)	5.9762 (2)
									^a 5.0523 (4)	^a 13.7854 (2)
									6.5942 (3)	5.9740 (3)
									^a 5.0430 (4)	^a 13.7549 (2)
									6.5918 (2)	5.9712 (4)
									^a 5.0424 (3)	^a 13.7552 (2)
1200 °C										
sample code	χ^2	R_p (%)	R_{Bragg}	ZrSiO ₄	weight fraction (%)				lattice data for ZrSiO ₄ and ^a α -Fe ₂ O ₃	
					Fe ₂ O ₃	t-ZrO ₂	m-ZrO ₂	c-SiO ₂	$a = b$ = axis (Å)	c = axis (Å)
5 FZS	2.498	07.58	03.48	83.89	2.68	5.14	4.16	4.12	6.6041 (2)	5.9815 (2)
	2.178	07.40	03.39	81.59	4.62	4.38	4.55	4.85	^a 5.0536 (3)	^a 13.7770 (2)
10 FZS	1.726	06.74	03.26	75.01	8.84	3.94	6.74	5.46	6.6008 (2)	5.9789 (2)
20 FZS	1.751	07.35	02.70	73.31	18.07	1.86	3.38	3.37	^a 5.0538 (1)	^a 13.7624 (5)
50 FZS	1.885	07.84	02.98	67.17	25.61	1.63	3.18	2.4	6.5996 (2)	5.9773(2)
75 FZS	1.992	08.84	04.28	57.84	30.85	2.43	5.45	3.42	^a 5.0537 (8)	^a 13.7752 (3)
100 FZS									6.5987 (2)	5.9768 (2)
									^a 5.0487 (4)	^a 13.7659 (2)
									6.5973 (2)	5.9742 (2)
									^a 5.0477 (3)	^a 13.7648 (1)
									6.5959 (2)	5.9718 (3)
									^a 5.0445 (3)	^a 13.7643(1)
1300 °C										
sample code	χ^2	R_p (%)	R_{Bragg}	ZrSiO ₄	weight fraction (%)				lattice data for ZrSiO ₄ and ^a α -Fe ₂ O ₃	
					Fe ₂ O ₃	t-ZrO ₂	m-ZrO ₂	c-SiO ₂	$a = b$ = axis (Å)	c = axis (Å)
5 FZS	2.573	07.95	04.18	87.54	2.31	3.37	3.95	2.82	6.6035 (2)	5.9812 (2)
10 FZS	2.240	07.59	03.48	80.13	4.16	2.50	4.30	8.90	^a 5.0565 (4)	^a 13.7112 (2)
20 FZS	1.972	07.14	03.75	75.79	8.25	3.11	5.52	7.32	6.6024 (2)	5.9796 (2)
50 FZS	2.081	08.09	03.31	76.01	19.62	-	2.64	1.72	^a 5.0570 (8)	^a 13.7838 (6)
75 FZS	2.024	08.32	03.27	71.73	26.51	-	0.89	0.86	6.5995 (2)	5.9772 (2)
100 FZS	1.667	08.36	04.26	65.68	33.12	-	0.63	0.56	^a 5.0517 (8)	^a 13.7654 (6)
									6.5982 (2)	5.9764 (2)
									^a 5.0463 (5)	^a 13.7651 (2)
									6.5970 (2)	5.9750 (2)
									^a 5.0492 (4)	^a 13.7690 (2)
									6.5954 (2)	5.9733 (2)
									^a 5.0483 (3)	^a 13.7794 (2)

^aIndicates the lattice data for α -Fe₂O₃.

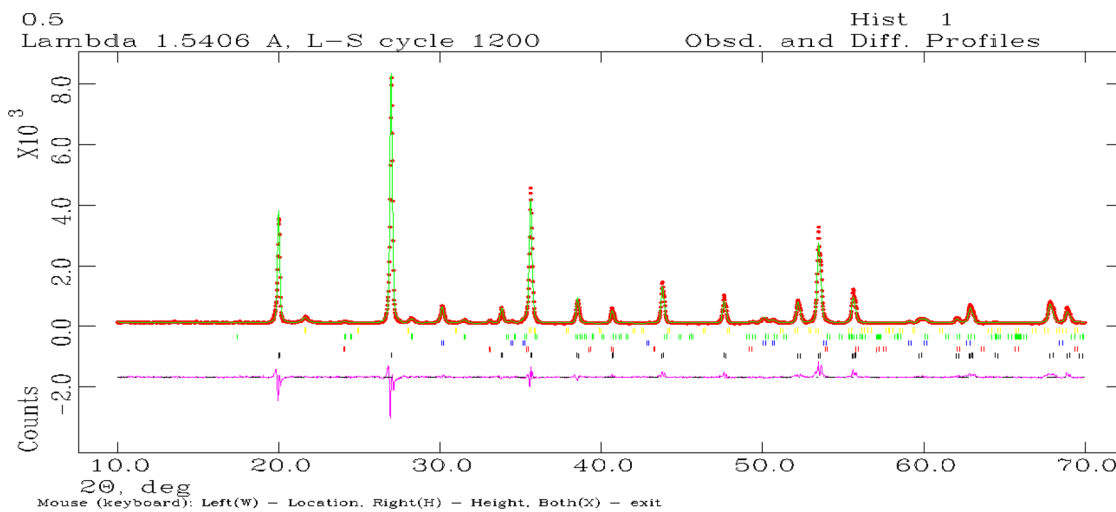


Figure 5. Refined powder diffraction patterns for SFZS sample at 1200 °C. (*red dotted lines, observed; solid green lines, calculated; and pink shows the difference.) Brag positions are indicated in vertical bars: black bars, red bars, blue bars, green bars, and yellow bars are correspondingly assigned for ZrSiO₄, α-Fe₂O₃, t-ZrO₂, m-ZrO₂, and c-SiO₂.

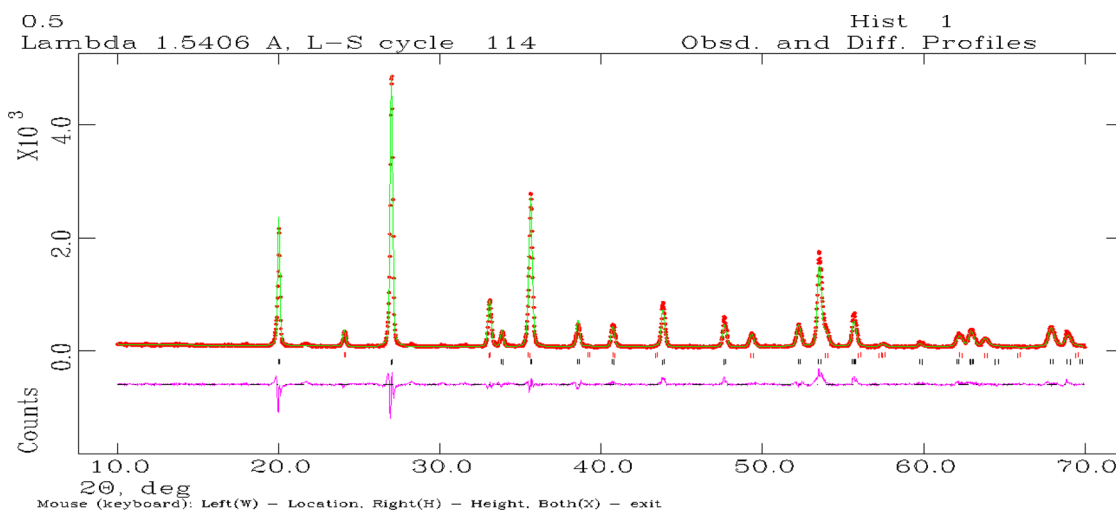


Figure 6. Refined powder diffraction patterns for 7SFZS sample at 1300 °C. (*red dotted lines, observed; solid green lines, calculated; and pink shows the difference.) Brag positions are indicated in vertical bars: black bars and red bars are correspondingly assigned for ZrSiO₄ and α-Fe₂O₃.

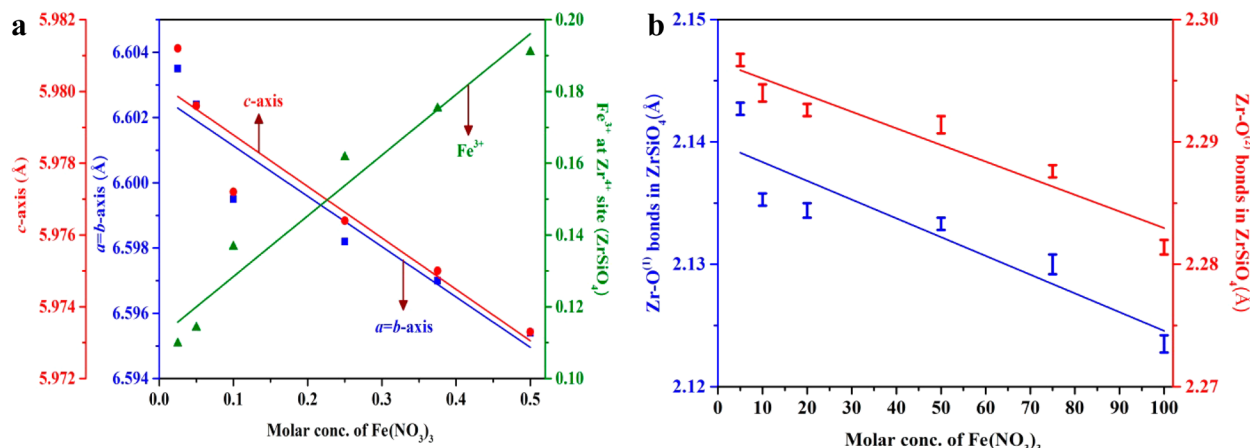


Figure 7. Behavior of lattice parameters (a), Fe³⁺ occupancy at ZrSiO₄ lattice (a), and trend in the behavior of selected bond lengths in ZrSiO₄ due to Fe³⁺ substitution (b).

Morphological Features. The surface morphological analysis (Figure 13) performed for 50FZS and 100FZS samples

reveal the densely crystallized structure of ZrSiO₄ and α-Fe₂O₃ composites. The average grain size is determined to be

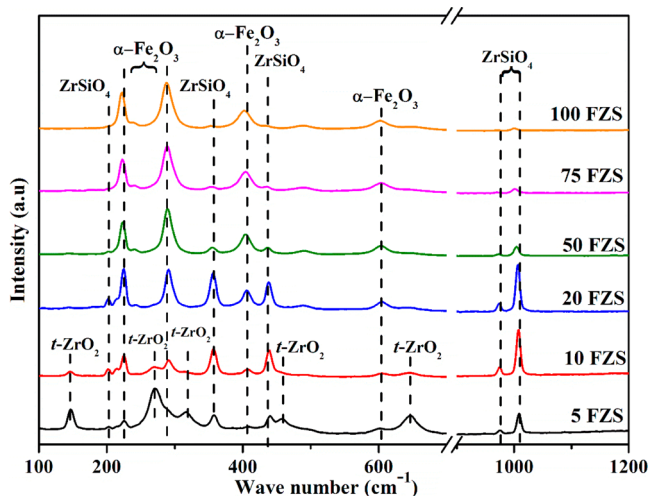


Figure 8. Raman spectra recorded for ZrSiO_4 - $\alpha\text{-Fe}_2\text{O}_3$ composite system at $1100\text{ }^\circ\text{C}$.

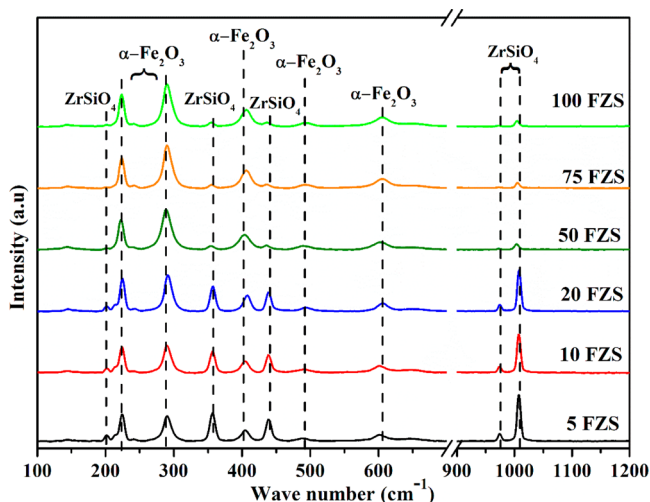


Figure 9. Raman spectra recorded for ZrSiO_4 - $\alpha\text{-Fe}_2\text{O}_3$ composite system at $1300\text{ }^\circ\text{C}$.

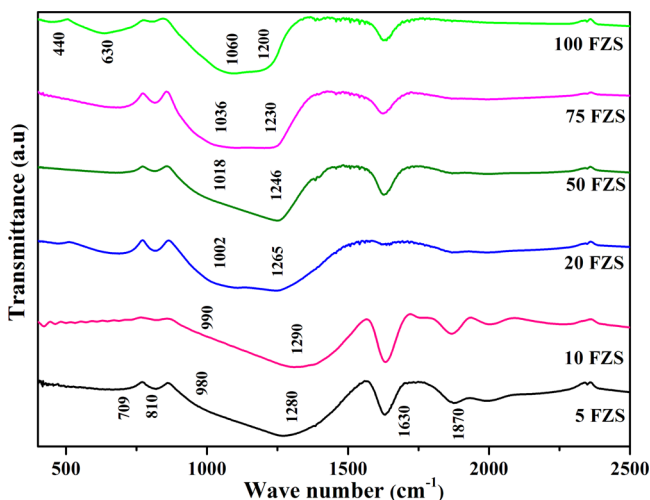


Figure 10. FT-IR spectra recorded for ZrSiO_4 - $\alpha\text{-Fe}_2\text{O}_3$ composite system at $900\text{ }^\circ\text{C}$.

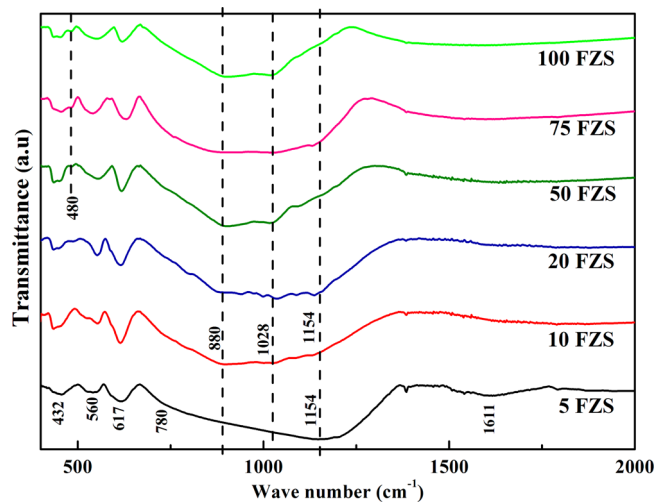


Figure 11. FT-IR spectra recorded for ZrSiO_4 - $\alpha\text{-Fe}_2\text{O}_3$ composite system at $1300\text{ }^\circ\text{C}$.

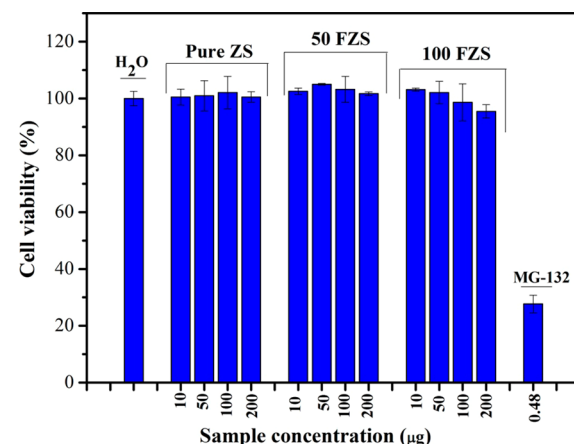


Figure 12. Percentage of viable cells with MG-63 cells treated on Pure ZS, 50 FZS, and 100 FZS.

approximately 800 nm which is due to the effect of heat treatment at $1300\text{ }^\circ\text{C}$. As the XRD results infer the presence of two distinct ZrSiO_4 and $\alpha\text{-Fe}_2\text{O}_3$ crystalline phases, the crystallization of grains happen to be as a single entity with no morphological evidence for the presence of other phases. The scanned images at a resolution of $1\text{ }\mu\text{m}$ reveal the uniform grain growth over the entire surface, and the images at a resolution of 300 nm reveal the grains with hexagonal orientation. The variation in $\alpha\text{-Fe}_2\text{O}_3$ content did not affect the grain size, as the grains in both the samples appear to have similar size and morphology. However, 50FZS sample exhibited more cracks on its surface on comparison with the 100FZS sample in which the cracks were found to be less significant (Supporting Information 1).

The EDX analysis were found to be in good agreement with the results of XRD, Raman, and FTIR. In order to confirm the existence of ZrSiO_4 and $\alpha\text{-Fe}_2\text{O}_3$ in a single grain, point EDX was obtained at three randomly selected points. The point EDX spectrum (Supporting Information 2) obtained for 100FZS sample, and their corresponding elemental analysis data signifies the presence of existing elements at all those random points. The elemental mapping for 100 FZS sample (Supporting Information 3) indicates the distribution of all the elements in the selected region. Oxygen is found uniformly

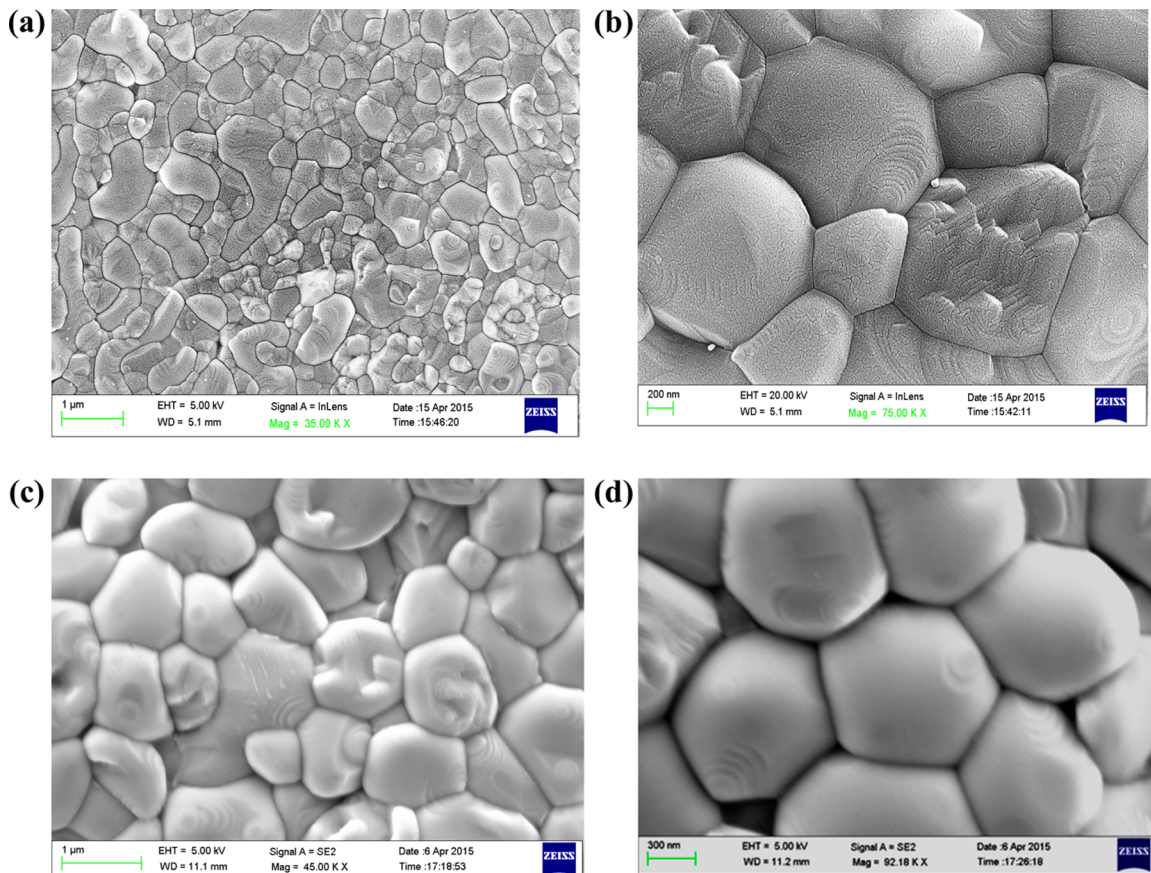


Figure 13. Surface morphological features determined at 1300 °C [13 (a) and 13(b) - 50FZS, 13 (c) and 13(d) - 100FZS].

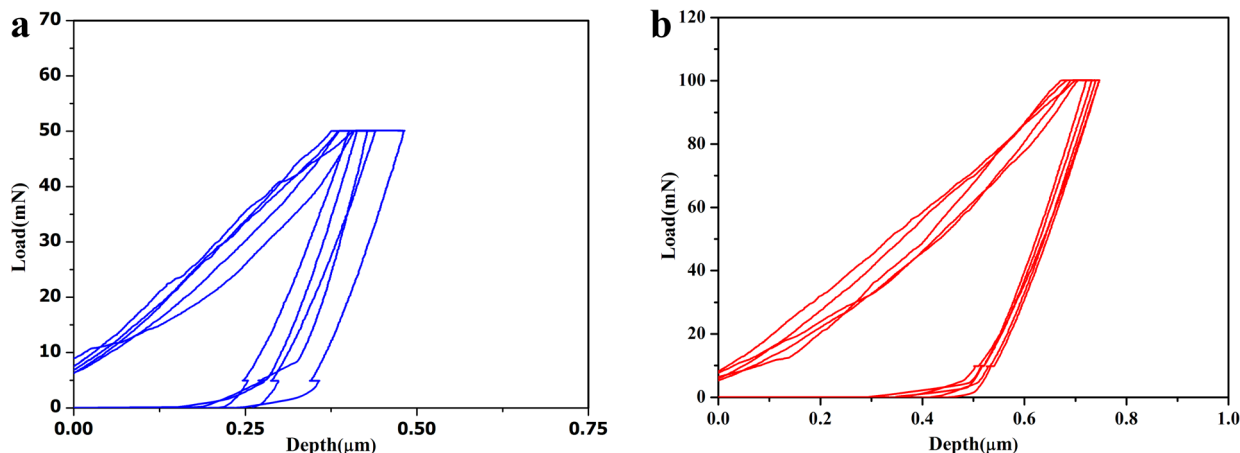


Figure 14. Load vs depth graphs determined by nanoindentation for 100 FZS sample.

distributed in all directions whereas Zr and Si appeared more dense at the top and Fe appeared more dense at the bottom. This clearly indicates the nucleation of ZrSiO_4 in the presence of $\alpha\text{-Fe}_2\text{O}_3$ forming a composite in a single grain.

Mechanical Tests. The load (mN) versus depth (μm) profiles of 100FZS is presented in Figure 14. The obtained mean values and standard deviation of Young's modulus and hardness at different loads for both 50FZS and 100FZS samples are presented in Table 3. The mechanical data of 100FZS sample indicated increased hardness and Young's modulus when compared to that of 50FZS sample. However, with increasing load from 50 mN to 100 mN, no significant change

Table 3. Mechanical Data Determined from Nano Indentation

load	mean hardness (GPa)		mean Young's modulus (GPa)	
	50FZS	100FZS	50FZS	100FZS
50 mN	1.56 (0.63)	7.83 (1.00)	74.07 (8.21)	183.14 (9.24)
100 mN	1.65 (0.37)	7.13 (0.18)	73.15 (7.37)	155.21 (6.03)

^aThe values indicated in the parentheses denote the \pm deviation from the mean value.

in the mechanical data is noticed for the investigated compositions.

■ DISCUSSION

The prevalence of ZrO_2 in three different forms, namely, monoclinic (stable from room temperature to 1170 °C), tetragonal (stable between 1170 and 2370 °C), and cubic (stable above 2370 °C) is well-known. Since the monoclinic to tetragonal phase transition is a reversible process it has been difficult to preserve a pure form of $t\text{-ZrO}_2$ phase at room temperature. Literature has evidenced the room temperature metastable $t\text{-ZrO}_2$ phase by the incorporation of metal oxides such as MgO , CaO , La_2O_3 , and Y_2O_3 .^{38–41} The mismatch in the valence effect between the substituted ions (Mg^{2+} , Ca^{2+} , La^{3+} , Y^{3+}) and Zr^{4+} tends to create oxygen vacancies and lattice deformations and hence forms $t\text{-ZrO}_2$ at room temperature. In the case of the biphasic system that comprises only $\text{SiO}_2\text{--ZrO}_2$ binary oxides, the $t\text{-ZrO}_2$ phase is preserved by the presence of amorphous SiO_2 matrix until 1100 °C.¹⁵ Beyond 1100 °C, the crystallization of amorphous SiO_2 to form $c\text{-SiO}_2$ leads to the degradation of $t\text{-ZrO}_2$ to $m\text{-ZrO}_2$.¹⁶ It is well-known that phase stability of $t\text{-ZrO}_2$ is maintained in the range between 1170 and 2370 °C, and during its cooling to room temperature, crack propagation leads to the conversion of $t\text{-ZrO}_2$ to yield $m\text{-ZrO}_2$. Hence, due to the crystallization of $c\text{-SiO}_2$ at 1200 °C, the metastable $t\text{-ZrO}_2$ was not able to be preserved during cooling at room temperature. The formation of pure ZrSiO_4 from the binary $\text{SiO}_2\text{--ZrO}_2$ oxide system is reported and it has been stated that the reaction between $t\text{-ZrO}_2$ and amorphous SiO_2 to form ZrSiO_4 occurs at high temperatures >1600 °C.^{42,43} The reason for the requirement of high temperature to form ZrSiO_4 is explained based on both crystallographic considerations and the high energy required for the interfacial reaction between $t\text{-ZrO}_2$ and SiO_2 .⁴⁴ Studies also reported that the reaction between $t\text{-ZrO}_2$ and SiO_2 to form ZrSiO_4 can be accelerated with the aid of suitable reaction promoters.^{45–48} Many studies have targeted the usage of iron as a promoter to stabilize ZrSiO_4 at lower temperatures. Alahakoon et al. obtained almost a single phase ZrSiO_4 at 1400 °C by using 5% iron as a dopant with no detection of iron oxide as a separate phase, and this means that Fe has entered the crystal lattice of ZrSiO_4 .⁴⁹ K.-R. Pyon and B.-H. Lee investigated the effect of iron as a dopant by varying its concentration from 5–30% and concluded that all the investigated compositions resulted in the formation of mixture of multiple phases, namely, $\alpha\text{-Fe}_2\text{O}_3$, ZrSiO_4 , $t\text{-ZrO}_2$, $m\text{-ZrO}_2$, and $c\text{-SiO}_2$ at 1300 °C.⁵⁰ Herrera et al. obtained solid solution of iron doped ZrSiO_4 at 1100 °C, and they also demonstrated that Fe^{3+} has occupied the tetrahedral lattice of ZrSiO_4 by replacing Si^{4+} ions.⁴⁶ The present study investigates the varying concentrations of Fe as a dopant ranging from 5% to 100% in $\text{SiO}_2\text{--ZrO}_2$ binary oxide system. It is seen from the results that at 800 °C the crystallization of $\alpha\text{-Fe}_2\text{O}_3$ is observed for the sample containing higher iron concentrations and the initiation of ZrSiO_4 crystallization is observed only at 1000 °C. An interesting observation is noted from the phase composition data derived from refinement that confirms rapid crystallization of ZrSiO_4 for the samples containing lower iron content, and the $\alpha\text{-Fe}_2\text{O}_3$ crystallization is observed only for the samples that contained higher iron content at 1000 °C. Such observations infer the crucial role of iron content in the promotion of interfacial reaction between amorphous SiO_2 and $t\text{-ZrO}_2$ to yield ZrSiO_4 . All the compositions witnessed an invariable degradation to form $m\text{-ZrO}_2$ at 1000 °C. A steady decline in the phase content of $t\text{-ZrO}_2$ with increasing $\alpha\text{-Fe}_2\text{O}_3$ presence is also noted at 1000 °C and this trend is observed during the

progressive heat treatment until 1300 °C. The complete absence of $t\text{-ZrO}_2$ is noted at 1300 °C for the samples containing higher $\alpha\text{-Fe}_2\text{O}_3$ content, namely, 50FZS, 75FZS, and 100FZS. Such $t\text{-ZrO}_2$ absence acknowledges the completion of reaction between SiO_2 and $t\text{-ZrO}_2$ to yield ZrSiO_4 .

It should be noted that the pure $\text{SiO}_2\text{--ZrO}_2$ system without any iron additions has not witnessed the formation of $m\text{-ZrO}_2$ and ZrSiO_4 crystallization at both 1000 and 1100 °C. However, in the case of $\text{SiO}_2\text{--ZrO}_2$ system with iron additions, three different important observations could be made at both 1000 and 1100 °C, namely, the rapid formation of ZrSiO_4 , the absence of $c\text{-SiO}_2$ crystallization, and the presence of $m\text{-ZrO}_2$ for all the investigated compositions. These inferences ascertain the crucial role of iron in promoting the interfacial reaction between amorphous SiO_2 and $t\text{-ZrO}_2$ to promote ZrSiO_4 crystallization. It has been reported that $t\text{-ZrO}_2$ stabilization is preserved by Si–O–Zr bonds in $\text{SiO}_2\text{--ZrO}_2$ system and any kind of bond rupture results in its degradation to yield $m\text{-ZrO}_2$ during cooling to room temperature.^{51,52} Since a sufficient amount of amorphous SiO_2 is consumed due to its reaction with $t\text{-ZrO}_2$ to promote ZrSiO_4 formation, the remaining system is left with negligible SiO_2 to preserve the Si–O–Zr bond network, and hence the formation of $m\text{-ZrO}_2$ could not be avoided at both 1000 and 1100 °C.

Heat treatments at 1200 to 1300 °C witnessed a gradual enhancement in the phase fractions that corresponds to the formation of ZrSiO_4 and a steady decline in the phase fraction of $t\text{-ZrO}_2$ for all the compositions. The crystallization of $c\text{-SiO}_2$ and the presence of $m\text{-ZrO}_2$ are observed at both 1200 and 1300 °C. Moreover, a steady enhancement in the $\alpha\text{-Fe}_2\text{O}_3$ content with respect to both the increment in the heat treatment temperature and enhanced iron additions is also noted. These observations confirm the influence of heat treatment on the crystallization of both ZrSiO_4 and $\alpha\text{-Fe}_2\text{O}_3$ phases. In the meanwhile, it is worth noting that heat treatment of pure $\text{SiO}_2\text{--ZrO}_2$ system at 1200 °C resulted in its almost complete degradation into $m\text{-ZrO}_2$. At 1300 °C, a maximum yield of 87.54% ZrSiO_4 is observed for the 5 FZS sample in which most of the $t\text{-ZrO}_2$ has reacted with amorphous SiO_2 . The ZrSiO_4 yield indicated a decreasing trend with the increased yield of $\alpha\text{-Fe}_2\text{O}_3$ phase. The complete absence of $t\text{-ZrO}_2$ is witnessed for the samples containing higher iron content and this infers the influence of heat treatment in promoting the reaction between $t\text{-ZrO}_2$ and amorphous SiO_2 to yield ZrSiO_4 . The influence of iron in the ZrSiO_4 formation is also confirmed from the strong reduction in the lattice parameters and this is mainly due to smaller Fe^{3+} occupying the Zr^{4+} positions at the ZrSiO_4 lattice. The occupancy of Fe^{3+} is also confirmed from the refined occupancy values which showed an increasing trend in occupancy with respect to the increased Fe^{3+} substitution. The gradual reduction in the selected bond lengths with increasing Fe^{3+} substitution at the ZrSiO_4 lattice is also established from the present results. The results also confirmed only the minimal inclusions of Fe^{3+} at the ZrSiO_4 lattice since the excess Fe^{3+} has led to its crystallization as $\alpha\text{-Fe}_2\text{O}_3$.

The results confirmed the rapid ZrSiO_4 crystallization for low iron concentrations at 1000 °C in comparison to the samples containing higher iron concentrations. The $\alpha\text{-Fe}_2\text{O}_3$ crystallization prior to the ZrSiO_4 crystallization can be a valid reason for maintaining the thermodynamic stability of the system by promoting slow and dense crystal growth of ZrSiO_4 , which in turn controls its dissociation to trace impurity phases.

An important observation that can be made from the Raman spectra for all the samples at 1100 and 1300 °C is the presence of significant peaks respective of $\alpha\text{-Fe}_2\text{O}_3$ even at low concentrations, namely, 5 FZS, 10 FZS, and 20 FZS. This may be due to the uniform dispersion of $\alpha\text{-Fe}_2\text{O}_3$ over the entire ZrSiO_4 matrix even at minor concentrations. The same can be correlated to the increase in intensity of the vibrational modes of $\alpha\text{-Fe}_2\text{O}_3$ for higher concentrations suppressing the number of intensity counts for ZrSiO_4 , and this is mainly attributed to the optical significance of $\alpha\text{-Fe}_2\text{O}_3$ over ZrSiO_4 . For higher concentrations (50 FZS, 75 FZS, and 100 FZS) due to high yield of $\alpha\text{-Fe}_2\text{O}_3$, ZrSiO_4 matrix may be clouded by the $\alpha\text{-Fe}_2\text{O}_3$ particles controlling the phase stability of ZrSiO_4 thereby reducing the occurrence of trace impurities like *t*- ZrO_2 , *m*- ZrO_2 , and *c*- SiO_2 . Hence, the existence of these trace impurities followed a reducing trend with increasing $\alpha\text{-Fe}_2\text{O}_3$ concentration as observed from the evidence of XRD and quantitative analysis. The stability of this composite system is a maximum for high iron containing samples (50 FZS, 75 FZS, and 100 FZS), as they detected a negligible amount of additional phases other than $\alpha\text{-Fe}_2\text{O}_3$ and ZrSiO_4 .

The broad IR stretching band observed in the region 980–1280 cm^{-1} at 900 °C is attributed to the presence of two different phases, namely, *t*- ZrO_2 and amorphous silica as confirmed from XRD. The shift in the observed band at 980 cm^{-1} toward higher frequencies and shift in the observed band at 1280 cm^{-1} toward lower frequencies with increasing iron concentrations is mainly due to the dominance of TO and LO asymmetric vibrational band of Si—O—Si over Zr—O—Si. Generally, the FT-IR bands at 440 and 630 cm^{-1} in 100 FZS sample are assigned for either ZrSiO_4 type units or Fe—O bond of $\alpha\text{-Fe}_2\text{O}_3$. In this case, such bands are assigned for Fe—O bond of $\alpha\text{-Fe}_2\text{O}_3$, since the crystallization of ZrSiO_4 has not yet started at 900 °C. The decreasing intensity of vibrational modes of SiO_2 network with increasing iron content witnessed at 1870 and 1960 cm^{-1} suggests the increasing asymmetry of the SiO_2 network. The FTIR spectrum of samples at 1300 °C corresponds to both crystallized ZrSiO_4 type units and $\alpha\text{-Fe}_2\text{O}_3$ showed good coincidence with the XRD data. The characteristic bands for all the trace phases like *t*- ZrO_2 , *m*- ZrO_2 , and *c*- SiO_2 that were visible in XRD is not detected in FTIR spectra as the characteristic bands for $\alpha\text{-Fe}_2\text{O}_3$ and ZrSiO_4 intends to quash the characteristic nature of trace phases. The shoulder band at 480 cm^{-1} , which is present in higher iron containing samples, that corresponds to the characteristics of $\alpha\text{-Fe}_2\text{O}_3$ indicates the formation of stable ZrSiO_4 and $\alpha\text{-Fe}_2\text{O}_3$ composite material as evident from XRD plots. The presence of this shoulder band at 480 cm^{-1} starting from 50FZS sample could also be correlated with the disappearance of trace phases due to the symbiotic crystallization of ZrSiO_4 and $\alpha\text{-Fe}_2\text{O}_3$ coordinating with one another in order to maintain the stability.

The uniform grain growth as observed from the FESEM images also suggest the dense crystallization of ZrSiO_4 and $\alpha\text{-Fe}_2\text{O}_3$ along with the supporting results obtained from XRD, Raman, and FTIR spectra. The crystallization in 100FZS sample is high when compared to the 50FZS sample as the grain size is high in 100FZS sample and the images also confirm the presence of dense fringes on the grains of 100FZS which were absent in 50FZS sample. At 1300 °C, this type of grain growth is expected, but the absence of different phases as individual grains supports the above deduction about coordinative crystallization of ZrSiO_4 and $\alpha\text{-Fe}_2\text{O}_3$. The EDX

and elemental mapping analysis also appears to be in close argument with the XRD data.

The stability of hardness and Young's modulus in the case of 100FZS sample can be correlated to the dense and perfect crystallization of ZrSiO_4 and $\alpha\text{-Fe}_2\text{O}_3$ together forming a stable entity as observed from the microstructure of 100FZS sample. The absence of fractures on the surface of the 100FZS sample also confirms the effect of $\alpha\text{-Fe}_2\text{O}_3$ additions in controlling the stability and crystallization of the composites. The presence of trace impurity phases and less densification of ZrSiO_4 and $\alpha\text{-Fe}_2\text{O}_3$ may be the reason for the low hardness and Young's modulus values of the 50FZS sample. The hardness and Young's modulus derived from 100FZS samples can be compared with the hardness values of different forms of ZrO_2 , which are generally used for dental and biomedical applications. Though few forms of ZrO_2 like commercially used PZT (Polycrystalline *t*- ZrO_2) show very high values of hardness up to 20 GPa and Young's modulus of about 200 GPa,^{53–55} the method of fabrication of commercial materials, chemical synthesis routes, stabilizing entities, morphology, and crystallization plays a major role in maintaining the mechanical stability of ZrO_2 .⁵⁶ In this case materials formed from a simple chemical sol–gel synthesis route have derived a novel ceramic whose hardness can be compared at a competitive level with many materials which are of commercial use in orthopedic and dental applications. The crystallization of $\alpha\text{-Fe}_2\text{O}_3$ along with ZrSiO_4 is also playing a crucial role in maintaining the cell viability and cell proliferation ability, thus qualifying it as a potent biomaterial. The crystallization of ZrSiO_4 and $\alpha\text{-Fe}_2\text{O}_3$ together with enhanced grain growth is playing a major role in maintaining the mechanical properties of the formed composite.

CONCLUSIONS

The following conclusions could be drawn from the present investigation: (1) A novel biphasic ceramic material containing phases of ZrSiO_4 and $\alpha\text{-Fe}_2\text{O}_3$ has been successfully formed at 1300 °C. (2) The iron content and heat treatments played major roles in controlling the thermodynamic stability of the system to promote the crystallization and densification of ZrSiO_4 along with $\alpha\text{-Fe}_2\text{O}_3$. (3) The occupancy of Fe^{3+} at the ZrSiO_4 lattice has promoted the interfacial reaction between amorphous SiO_2 and *t*- ZrO_2 to yield crystallized ZrSiO_4 . The Fe^{3+} occupancy at the ZrSiO_4 lattice has been found to be selective and the excess Fe^{3+} has crystallized in the form of $\alpha\text{-Fe}_2\text{O}_3$. (4) These formed composites exhibited good biocompatible features and significant mechanical characteristics like hardness and Young's modulus, which make this a promising material for use as a bone or dental implant where the demands for high mechanical strength are necessitated. (5) The results from the investigation have also paved the way for exploring the possibility of fabricating a 3D scaffold material for tissue engineering applications.

ASSOCIATED CONTENT

Supporting Information

Fractures on the surfaces of 50FZS and 100FZS samples that are heat-treated to 1300 °C; point EDX spectrum images obtained for 100FZS at 1300 °C; elemental mapping images of the 100FZS sample at 1300 °C. The Supporting Information is available free of charge on the ACS Publications website at DOI: 10.1021/acs.cgd.Sb00677.

AUTHOR INFORMATION

Corresponding Author

*E-mail: para_kanna@yahoo.com. Phone: 0091-413-2654973.

Notes

The authors declare no competing financial interest.

ACKNOWLEDGMENTS

The authors are thankful to the financial support received from the Council of Scientific and Industrial Research, India (CSIR Scheme No. 22(612)/12/EMR-II). The Instrumentation facility availed from the Central Instrumentation Facility (CIF) of Pondicherry University is greatly acknowledged. The support from Dr.Arunkumar Dhayalan, Department of Biotechnology, Pondicherry University for supporting cytotoxicity analysis is gratefully acknowledged.

REFERENCES

- (1) Cortes, E. C.; de la Fuente, J. A. M.; Moreno, J. M. Solid-Solution Formation in the Synthesis of Fe-Zircon. *J. Am. Ceram. Soc.* **2004**, *87*, 612–616.
- (2) Veytizou, C.; Quinson, J.-F.; Douy, A. Sol-gel synthesis via an aqueous semi-alkoxide route and characterization of zircon powders. *J. Mater. Chem.* **2000**, *10*, 365–370.
- (3) Suzuki, M.; Sodeoka, S.; Inoue, T. Structure Control of Plasma Sprayed Zircon Coating by Substrate Preheating and Post Heat Treatment. *Mater. Trans.* **2005**, *46*, 669–674.
- (4) Parcianello, G.; Bernardo, E.; Colombo, P. Low temperature synthesis of zircon from silicone resins and oxide nano-sized particles. *J. Eur. Ceram. Soc.* **2012**, *32*, 2819–2824.
- (5) Zhao, F.; Li, W.; Luo, H. Sol-gel modified method for obtention of gray and pink ceramic pigments in zircon matrix. *J. Sol-Gel Sci. Technol.* **2009**, *49*, 247–252.
- (6) Mountjoy, G.; Pickup, D. M.; Anderson, R.; Wallidge, G. W.; Holland, M. A.; Newport, R. J.; Smith, M. E. Changes in the Zr environment in zirconia-silica xerogels with composition and heat treatment as revealed by Zr K-edge XANES and EXAFS. *Phys. Chem. Chem. Phys.* **2000**, *2*, 2455–2460.
- (7) Berry, F. J.; Eadon, D.; Holloway, J.; Smart, L. E. Iron-doped zirconium silicate. *J. Mater. Chem.* **1996**, *6*, 221–225.
- (8) Berry, F. J.; Eadon, D.; Holloway, J.; Smart, L. E. Iron-doped zircon: The mechanism of formation. *J. Mater. Sci.* **1999**, *34*, 3631–3638.
- (9) Ardizzone, S.; Cappelletti, G.; Fermo, P.; Oliva, C.; Scavini, M.; Scimè, F. Structural and spectroscopic investigations of blue, vanadium-doped $ZrSiO_4$ pigments prepared by a sol-gel route. *J. Phys. Chem. B* **2005**, *109*, 22112–22119.
- (10) Royer, R. A.; Burgos, W. D.; Fisher, A. S.; Unz, R. F.; Dempsey, B. A. Enhancement of Biological reduction of Hematite by Electronshuttling and Fe(II) Complexation. *Environ. Sci. Technol.* **2002**, *36*, 1939–1946.
- (11) Jia, Z.; Liu, J.; Wang, Q.; Li, S.; Qi, Q.; Zhu, R. Synthesis of 3D hierarchical porous iron oxides for adsorption of Congo red from dye waste water. *J. Alloys Compd.* **2015**, *622*, 587–595.
- (12) Hosseini-Zori, M.; Taheri-Nassaj, E. Nano encapsulation of hematite into silica matrix as a red inclusion ceramic pigment. *J. Alloys Compd.* **2011**, *510*, 83–86.
- (13) Heydari, H.; Naghizadeh, R.; Samimbanihashemi, H. R.; Hosseini Zori, M. Synthesis and characterisation of hematite-zircon nanocomposite by sol-gel method. *Adv. Mater. Res.* **2013**, *829*, 544–548.
- (14) Hosseini-Zori, M. Microstructure of nanoscale hematite encapsulated by zircon and cristobalite in ceramic pigment and examination of glazes application. *J. Adv. Microsc. Res.* **2013**, *8*, 61–66.
- (15) Vasanthavel, S.; Nandha Kumar, P.; Kannan, S. Quantitative Analysis on the Influence of SiO_2 Content on the Phase Behavior of ZrO_2 . *J. Am. Ceram. Soc.* **2014**, *97*, 635–642.
- (16) Behera, P. S.; Vasanthavel, S.; Ponnivan, V.; Kannan, S. Influence of gadolinium content on the tetragonal to cubic phase transition in zirconia-silica binary oxides. *J. Solid State Chem.* **2015**, *225*, 305–309.
- (17) Larson, A. C.; Von Dreele, R. B. General Structure Analysis System (GSAS); Los Alamos National Laboratory Report LAUR, 2004; pp 86748.
- (18) Toby, B. H. EXPGUI, a graphical user interface for GSAS. *J. Appl. Crystallogr.* **2001**, *34*, 210–213.
- (19) Hazen, R. M.; Finger, L. W. Crystal structure and compressibility of Zircon at high pressure. *Am. Mineral.* **1979**, *64*, 196–201.
- (20) Blake, R. L.; Hessevick, R. E. Refinement of the Hematite Structure. *Am. Mineral.* **1966**, *51*, 123–129.
- (21) Howard, C. J.; Hill, R. J.; Reichert, B. E. Structures of the ZrO_2 polymorphs at room temperature by high-resolution neutron powder diffraction. *Acta Crystallogr., Sect. B: Struct. Sci.* **1988**, *44*, 116–120.
- (22) Smith, D. K.; Newkirk, H. W. The Crystal Structure of Baddeleyite (Monoclinic ZrO_2) and its relation to the Polymorphism of ZrO_2 . *Acta Crystallogr.* **1965**, *18*, 983–991.
- (23) Dera, P.; Lazar, J. D.; Prakapenka, V. B.; Barkley, M.; Downs, R. T. New insights into the high-pressure polymorphism of SiO_2 cristobalite. *Phys. Chem. Miner.* **2011**, *38*, 517–529.
- (24) ISO 10993–5: Biological evaluation of medical devices-Part 5: Tests for cytotoxicity: International organization for standardization.
- (25) Cree, Ian A., Ed. cancer cell culture: methods and protocolsMethods Mol. Biol., 2nd ed.; Methods in Molecular Biology, 2011; Vol 731, pp 237–245.
- (26) Yan, X.-B.; Yang, D.-S.; Gao, X.; Feng, J.; Shi, Z.-L.; Ye, Z. Caspase-8 dependent osteosarcoma cell apoptosis induced by proteasome inhibitor MG132. *Cell Biol. Int.* **2007**, *31*, 1136–1143.
- (27) Oliver, W. C.; Pharr, G. M. An improved technique for determining hardness and elastic modulus using load and displacement sensing indentation experiments. *J. Mater. Res.* **1992**, *7*, 1564–1583.
- (28) Vasanthavel, S.; Kannan, S. Phase stabilization of ZrO_2 polymorph by combined additions of Ca^{2+} and PO_4^{3-} ions through an in situ synthetic approach. *J. Am. Ceram. Soc.* **2014**, *97*, 3774–3780.
- (29) Gucsik, A.; Zhang, M.; Koeberl, C.; Salje, E. K. H.; Redfern, S. A. T.; Pruneda, J. M. Infrared and Raman spectra of $ZrSiO_4$ experimentally shocked at high pressures. *Mineral. Mag.* **2004**, *68*, 801–811.
- (30) Nasdala, L.; Zhang, M.; Kempe, U.; Panczer, G.; Gaft, M.; Andrus, M.; Plötz, M. Spectroscopic methods applied to zircon. In *Reviews in Mineralogy and Geochemistry*, Hanchar, J. M.; Hoskin, P. W. O., Eds.; Mineralogical Society of America: Washington. DC, 2003; Vol 53, pp 427–467.
- (31) de Faria, D. L. A.; Lopes, F. N. Heated goethite and natural hematite: Can Raman spectroscopy be used to differentiate them? *Vib. Spectrosc.* **2007**, *45*, 117–121.
- (32) Gotic, M.; Music, S. Mossbauer, FT-IR and FE-SEM investigation of iron oxides precipitated from $FeSO_4$ solutions. *J. Mol. Struct.* **2007**, *834*–836, 445–453.
- (33) Herrera, G.; Montoya, N.; Alarcón, J. Microstructure of Fe-ZrSiO₄ solid solutions prepared from gels. *J. Eur. Ceram. Soc.* **2012**, *32*, 227–234.
- (34) Varghese, J.; Joseph, T.; Sebastian, M. T. ZrSiO₄ ceramics for microwave integrated circuit applications. *Mater. Lett.* **2011**, *65*, 1092–1094.
- (35) Sarath Chandra, V.; Baskar, G.; Suganthi, R. V.; Elayaraja, K.; Ahymah Joshy, M. I.; SofiBeaula, W.; Mythili, R.; Venkatraman, G.; Narayana Kalkura, S. Blood Compatibility of Iron-Doped Nanosize Hydroxyapatite and Its Drug Release. *ACS Appl. Mater. Interfaces* **2012**, *4*, 1200–1210.
- (36) Yiu, H. H. P.; Keane, M. A.; Lethbridge, Z. A. D.; Lees, M. R.; El Haj, A. J.; Dobson, J. Preparation and characterization of iron oxide–silica composite particles using mesoporous sba-15 silica as template and their internalization into mesenchymal stem cell and human bone cell lines. *Nanotechnology* **2010**, *9*, 165–170.

- (37) Brunner, T. J.; Wick, P.; Manser, P.; Spohn, P.; Grass, R. N.; Limbach, L. K.; Bruinink, A.; Stark, W. J. In Vitro Cytotoxicity of Oxide Nanoparticles: Comparison to Asbestos, Silica, and the Effect of Particle Solubility. *Environ. Sci. Technol.* **2006**, *40*, 4374–4381.
- (38) Scott, H. G. Phase Relationships in the Zirconia-Yttria System. *J. Mater. Sci.* **1975**, *10*, 1527–1535.
- (39) Garvie, R. C.; Nicholson, P. S. Structure and Thermodynamical Properties of Partially Stabilized Zirconia in the CaO–ZrO₂ System. *J. Am. Ceram. Soc.* **1972**, *55*, 152–157.
- (40) Garvie, R. C.; Urbani, C.; Kennedy, D. R.; Mcneuer, J. C. Biocompatibility of Magnesia Partially Stabilized Zirconia (Mg–Psz) Ceramics. *J. Mater. Sci.* **1984**, *19*, 3224–3228.
- (41) Thangadurai, P.; Chandra Bose, A.; Ramasamy, S. Phase Stabilization and Structural Studies of Nanocrystalline La₂O₃–ZrO₂. *J. Mater. Sci.* **2005**, *40*, 3963–3968.
- (42) Suarez, G.; Acevedo, S.; Rendtorff, N. M.; Garrido, L. B.; Aglietti, E. F. Colloidal processing, sintering and mechanical properties of zircon (ZrSiO₄). *Ceram. Int.* **2015**, *41*, 1015–1021.
- (43) Ebadzadeh, T.; Valefi, M. Microwave-assisted sintering of zircon. *J. Alloys Compd.* **2008**, *448*, 246–249.
- (44) Newton, R. C.; Manning, C. E. Gibbs free energy of formation of zircon from measurement of solubility in H₂O. *J. Am. Ceram. Soc.* **2005**, *88*, 1854–1858.
- (45) Cappelletti, G.; Ardizzone, S.; Fermo, P.; Gilardoni, S. The influence of iron content on the promotion of the zircon structure and the optical properties of pink coral pigments. *J. Eur. Ceram. Soc.* **2005**, *25*, 911–917.
- (46) Herrera, G.; Montoya, N.; Alarcon, J. Synthesis and Characterization of Iron-doped ZrSiO₄ solid Solutions from Gels. *J. Am. Ceram. Soc.* **2011**, *94*, 4247–4255.
- (47) Cannio, M.; Bondioli, F. Mechanical activation of raw materials in the synthesis of Fe₂O₃-ZrSiO₄ inclusion pigment. *J. Eur. Ceram. Soc.* **2012**, *32*, 643–647.
- (48) Ardizzone, S.; Binaghi, L.; Cappelletti, G.; Fermo, P.; Gilardoni, S. Iron doped zirconium silicate prepared by a sol-gel procedure. The effect of the reaction conditions on the structure morphology and optical properties of the powders. *Phys. Chem. Chem. Phys.* **2002**, *4*, 5683–5689.
- (49) Alahakoon, W. P. C. M.; Burrows, S. E.; Howes, A. P.; Karunaratne, B. S. B.; Smith, M. E.; Dobedoe, R. Fully densified zircon co-doped with iron and aluminium prepared by sol-gel processing. *J. Eur. Ceram. Soc.* **2010**, *30*, 2515–2523.
- (50) Pyon, K.-R.; Lee, B.-H. Effect of iron content and annealing temperature on the color characteristics of Fe-ZrSiO₄ coral pigments by sol-gel method. *J. Ceram. Soc. Jpn.* **2009**, *117*, 258–263.
- (51) del Monte, F.; Larsen, W.; Mackenzie, J. D. Chemical interactions promoting the ZrO₂ tetragonal stabilization in ZrO₂-SiO₂ binary oxides. *J. Am. Ceram. Soc.* **2000**, *83*, 1506–1512.
- (52) del Monte, F.; Larsen, W.; Mackenzie, J. D. Stabilization of tetragonal ZrO₂ in ZrO₂-SiO₂ binary oxides. *J. Am. Ceram. Soc.* **2000**, *83*, 628–634.
- (53) Piconi, C.; Maccauro, G. Zirconia as a ceramic biomaterial. *Biomaterials* **1999**, *20*, 1–25.
- (54) Alao, A.-R.; Yin, L. Nano-scale mechanical properties and behaviour of presintered zirconia. *J. Mech. Beh. Biomed. Mater.* **2014**, *36*, 21–31.
- (55) Shao, L.; Jiang, D.; Gong, J. Nanoindentation Characterization of the Hardness of Zirconia Dental Ceramics. *Adv. Eng. Mater.* **2013**, *15*, 704–707.
- (56) Denry, I.; Kelly, J. R. Emerging Ceramic-based Materials for Dentistry. *J. Dent. Res.* **2014**, *93*, 1235–1242.